3D shear wave velocity structure in the southwestern Okinawa Trough

Weiwei Wang[1,2], Shu-Huei Hung[2], Martha K. Savage[1], Yinhe Luo[3], Xin Zhang[4], Andrew Curtis[4], Spahr Webb[5], Ban-Yuan Kuo[6], Tim Stern[1], Xiaozhou Yang[3], Jinyun Xie[3], Hsin-Ying Yang[2], Pei-Ying Patty Lin[7], Chau-Chang Wang[8,9], Ching-Ren Lin[6]

[1]Victoria University of Wellington, Wellington, New Zealand

[2]National Taiwan University, Taipei, Taiwan

[3]China University of Geosciences (Wuhan), Wuhan, China

[4]The University of Edinburgh, Edinburgh, UK

[5]Lamont-Doherty Earth Observatory, Columbia University, Palisades, NY, USA

[6]Institute of Earth Sciences, Academia Sinica, Taipei, Taiwan

[7]National Taiwan Normal University, Taipei, Taiwan

[8]National Sun Yat-Sen University, Kaohsiung, Taiwan

[9]Taiwan Ocean Research Institute, Kaohsiung, Taiwan

This paper is a non-peer reviewed preprint submitted to EarthArXiv.

Corresponding author: Weiwei Wang, weiwei.wang204@hotmail.com

Abstract

The southwestern Okinawa Trough is an active back-arc basin, extending and rifting within the continental lithosphere. Studying the southwestern Okinawa Trough is important for understanding the processes involved in the opening and development of a back-arc basin. At various times between 2010 and 2018, the Institute of Earth Sciences, Academia Sinica, Taiwan deployed 34 Ocean Bottom Seismometers (OBSs) over a region $\sim 0.2°\times0.3°$ in longitude/latitude on the southwest edge of Okinawa Trough offshore northeast Taiwan. Ambient noise recorded on vertical velocity and pressure sensors is used to retrieve Rayleigh/Scholte waves to study the subseafloor shear wave velocity structure. A reference phase velocity dispersion curve is forward-modeled, according to a shear velocity model from an adjacent site determined by *Kuo et al.* (2015). Phase velocity dispersion curves are measured from the retrieved Rayleigh/Scholte waves and unwrapped according to which branch of the modeled phase velocities they appear closest to. Applying a 3D Monte Carlo inversion, shear wave velocities are estimated to $\sim$ 4 km depth using the obtained frequency-dependent phase velocities. A low velocity in the basin centre indicates the back-arc rifting is active at the southwest edge of Okinawa Trough. A comparison to the sites studied by *Kuo et al.* (2015) in the east of our study region suggests that back-arc rifting and extension may taper from east to west towards Taiwan.

1 Introduction

Taiwan is located on the convergent margin between the Eurasian Plate (EP) and Philippine Sea Plate (PSP; Figure 1 inset). In eastern offshore Taiwan, the Philippine Sea Plate subducts under the Eurasian Plate along the Ryukyu Trench (RT), forming the Ryukyu Arc and Okinawa Trough (OT) behind it (*Sibuet and Hsu*, 2004; *Ramsey et al.*, 2006). The Philippine Sea Plate is converging toward the Eurasian Plate at a rate of about $82mm/yr$ in a NW-SE direction and obliquely descending beneath the southwestern edge of the Ryukyu Trench (*Seno et al.*, 1993), and the Ryukyu Arc concomitantly retreats southwards at a rate of about $70mm/yr$ (*Nakamura*, 2004).

The Okinawa Trough is a curved back-arc basin where the most notable tectonic processes are active extension and rifting within the continental lithosphere. The estimated rates of the extension are 1–5 cm/yr (*Sibuet et al.*, 1998; *Nishimura et al.*, 2004). Continental rifting along the axis of the Okinawa Trough has occurred in three phases (*Sibuet et al.*, 1995). The first rifting phase started in the Middle Miocene (12 Ma) or Late Miocene (6 Ma), causing the most significant extension of 50 to 75 km. The second and third rifting phases occurred in the Late Pliocene-Pleistocene and Late Pleistocene to recent, involving an extension of 25 to 30 km in total. Rifting within the continental lithosphere is important for lithospheric evolution in an extensional stress condition. It can widen back-arc basins, increase sedimentary accumulation, and potentially lead to the breakup of continental lithosphere (*Kearey et al.*, 2009). The continental lithosphere in the central and southern Okinawa Trough has been ruptured along the rifting axis, and new oceanic crust has been created at the rifting centre since 2 Ma (*Liu et al.*, 2016). Back-arc extension is believed to have started recently (upper Pleistocene) in a N-S direction (*Sibuet et al.*, 1998; *Shyu and Liu*, 2001), and both rifting and extension of the Okinawa Trough have enhanced the Philippine Sea Plate subduction rate. Compared with global passive continental margins and marginal basins in the West Pacific, it is suggested that the central and southern Okinawa Trough is at the early

stage of seafloor spreading in which magma from decompression melting of upper mantle rocks ascends to form new oceanic crust at the spreading centre, while the northern Okinawa Trough is still at the mature stage of continental rifting and so not yet involved with volcanism and oceanic crust formation (*Liu et al.*, 2016). Previous studies on the helium isotopes of volcanic rocks indicated that the southern Okinawa Trough spreads faster than the central Okinawa Trough (*Yu et al.*, 2016).

The southern Okinawa Trough exhibits low velocity anomaly in the shallow depth ($< 20km$). The southern Okinawa Trough rapidly tapers towards the west and ends at the Yilan Plain (Figure 1) in northeast Taiwan, which may signify onshore rifting of the back-arc basin (*Sibuet et al.*, 1987). *Chou et al.* (2009) observed low velocity (both Vp and Vs) and low seismicity under the Yilan Plain. The 3D P wave velocity structure under northeast Taiwan imaged by local earthquakes (*Su et al.*, 2019) exhibits a low Vp beneath Yilan Plain, which appears to originate from an eastern offshore low Vp region, demonstrating Yilan Plain is the end of the Okinawa Trough opening. The crustal thickness in the southwestern Okinawa Trough is about 25 km (*Han et al.*, 2007; *Jia and Sun*, 2021) and the depth to the top of the slab is around 125 km (*Chou et al.*, 2006). Heat flow measurements (about 110 mW/m^2 on average, varying from 9 to 437 mW/m^2; *Shyu and Liu*, 2001) in the southwestern Okinawa Trough are high and are related to continental rifting and seafloor spreading (*Liu et al.*, 2016; *Chen et al.*, 2020). High heat flows (*Yamano et al.*, 1989; *Kinoshita and Yamano*, 1997; *Shyu and Liu*, 2001) indicate continuous spreading in the southern Okinawa Trough.

The Kuroshio (Black) Current is the biggest western boundary surface current in the western Pacific for its high speed, great depth and width. To study the Kuroshio Current, Ocean Drilling Program (ODP) Site 1202 was drilled at $24°48.24'N$, $122°30.00'E$ (*Salisbury*, 2002), within our study region (Figure 1). Four holes were drilled, providing peak shear strength down to 120 meters below the seafloor, Vp down to 15 meters below the seafloor, and density down to 140 meters below the seafloor. The local sedimentation rate is extremely high, possibly in excess of 3 m/k.y. (*Salisbury*, 2002), and a seismic profile (*Sibuet et al.*, 1998) in the same region was characteristic of a low-energy environment with muddy deposits.

Chou et al. (2009) observed low Vp, Vs, and high Vp/Vs in the fore-arc above the interface and interpreted them as serpentinization of the peridotitic mantle. *Ko et al.* (2012) suggested a cold mantle wedge at the southwest end of the Ryukyu subduction system according to significantly increased Q values in the edge zone measured from earthquake data recorded by OBSs and on-land stations. They proposed the high Q values are due to low temperatures and maybe low water content, which may result from a strong coupling between the slab edge and the Eurasian lithosphere. *Kuo et al.* (2012) applied shear-wave splitting to local earthquakes recorded by OBSs and on-land stations and observed along-trough variation of crustal anisotropy - the strength decreasing from the east to west. This is consistent with the scenario that the crack development is progressively weakened as the back-arc rifting tapers towards the west. *Lin and Kuo* (2013) applied numerical subduction models which demonstrate the tapering of Okinawa Trough toward Taiwan is not just a morphological feature but a lithospheric structure. The lithosphere is not only thinned across the axis by rifting but also thickened in response to the diminishing of the rifting towards Taiwan. *Kuo et al.* (2015) measured seafloor compliance and

inverted for crustal shear velocities under two sites (S002 and S005) in the southwestern Okinawa Trough and one site (EOS1) on the Ryukyu arc (Figure 1 inset). The results demonstrate a lower upper crustal shear velocity and a higher Vp/Vs in the trough site than in the arc site. This variation suggests that the upper continental crust in the southwestern Okinawa Trough is highly faulted and hydrated during rifting. The higher shear velocity under EOS1 characterizes the continental arc. Within the southwestern Okinawa Trough, the shear velocity increases from the east (S005) to the west (S002). It is likely that the crust has been stretched and faulted more significantly on S005 than on S002, as a result of more active rifting. Using seismic ambient noise data, this study will reveal whether the shear velocity continues increasing towards the west, which would mean the rifting becomes less active from the centre to the edge of the back-arc.

2 Data and method

2.1 Data

From 2010 to 2018, the Institute of Earth Sciences (IES), Taiwan, deployed 34 OBSs at different times (Figure 1) in the southwestern Okinawa Trough. The deployment and instrument information can be found in supplementary Tables S1–S2 and Figures S1–S2.

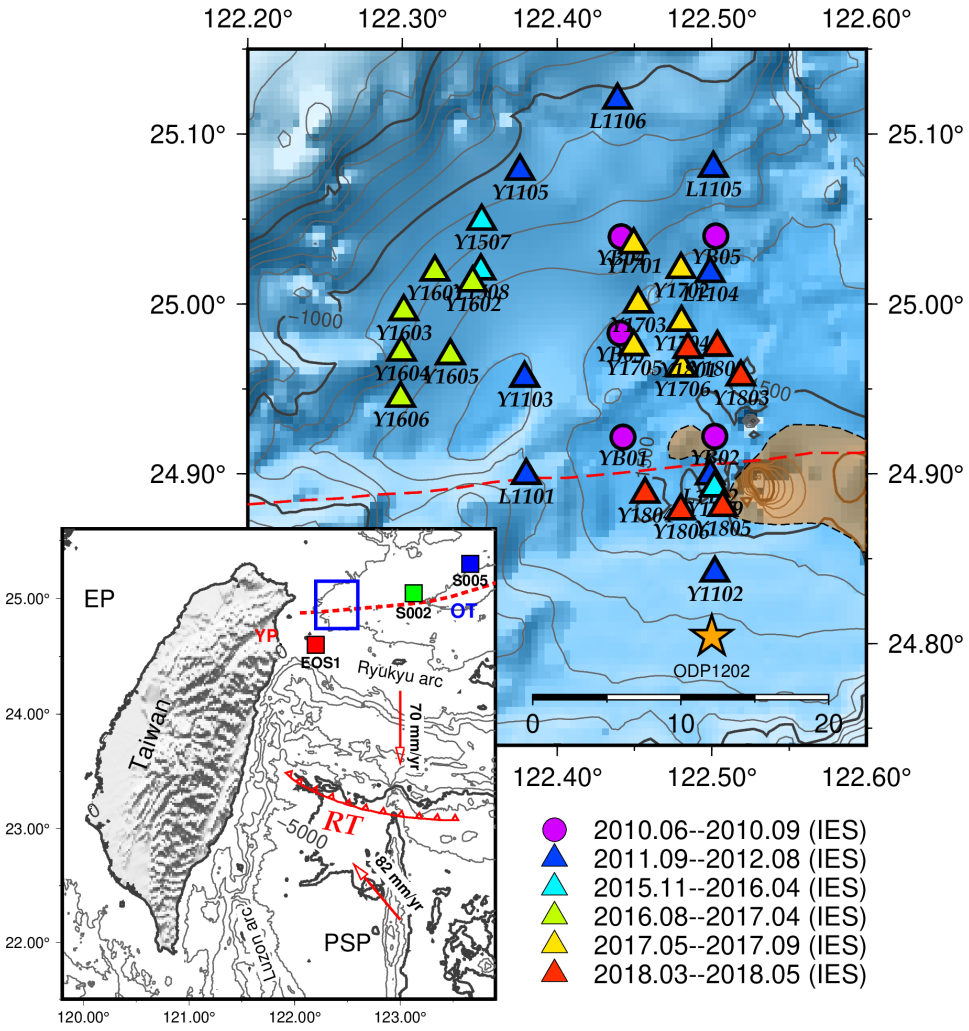

Figure 1. Deployment of Ocean Bottom Seismometers (OBSs) in the southwestern Okinawa Trough. 34 Ocean Bottom Seismometers (OBSs) were deployed at different times, denoted by different colors. Circles indicate the instruments equipped with 3-component seismometers only; triangles indicate the instruments equipped with differential pressure gauges and 3-component seismometers. The red dashed line denotes the rifting axis of Okinawa Trough (*Sibuet et al.*, 1998). The orange star shows the position of ODP1202 (*Salisbury*, 2002). Orange shades mark volcanic outcrops or slightly buried volcanism (*Sibuet et al.*, 1998) in the study region. The blue rectangle in the inset outlines our region of study. The Okinawa Trough terminates at Yilan plain (*Sibuet et al.*, 1987; *Chou et al.*, 2009; *Su et al.*, 2019). Three stations (EOS1, S002, S005) used in *Kuo et al.* (2015) are plotted. OT, Okinawa Trough; YP, Yilan Plain; RT, Ryukyu Trench. EP, Eurasian Plate; PSP, Philippine Sea Plate.

2.2 Ambient noise cross-correlations

Station pair cross-correlations are computed on both differential pressure gauges and seismic vertical continuous data, using MSnoise (*Lecocq et al.*, 2014). Figure 2 shows the cross-correlations derived from pressure gauges and seismic vertical components. The arrivals are considered to be Rayleigh-type Scholte waves. Rayleigh waves, including both radial and vertical motions, are surface waves propagating on a solid-solid interface, while Scholte waves have the same physical properties but propagate on a fluid-solid interface. From both seismic vertical channels and pressure gauges, clear Scholte waves are retrieved and show similar fundamental mode arrivals. For each station pair, the cross-correlation function with clearer signals, after comparing the seismic vertical channels and pressure gauges, is used. For station pairs without pressure gauges equipped, cross-correlations derived from seismic vertical components are used. The red dashed lines bracket the fundamental mode arrivals. *Wang* (2022) (Section 5.6.1) demonstrated the earlier arrivals (marked by blue shades in Figure 2), dominated at 1–3 s period band, are likely to be a mixture of multiple higher modes traveling in the sub-seafloor sediments (*Nolet and Dorman*, 1996) and, therefore, these are not used in the following analysis (phase velocity measurement and inversion).

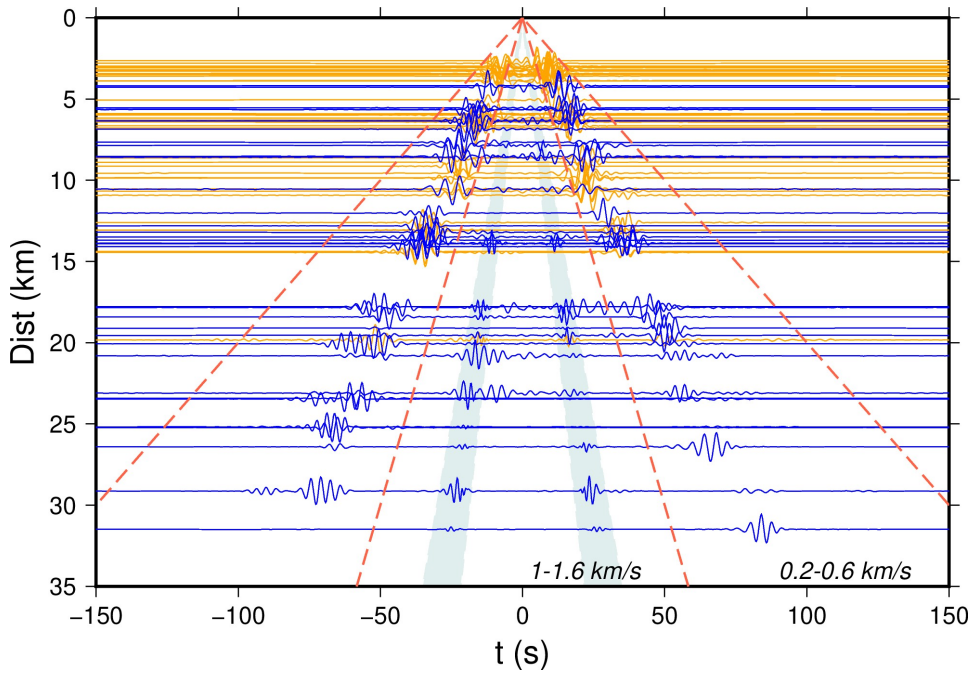

Figure 2. 75 station pair cross-correlation functions with clear signals computed using the pressure gauges (blue) or seismic vertical components (orange) of the OBSs, plotted as a function of interstation distance, filtered at 1–20 s, showing an earlier arrival with a dominant period of 1–3 s and a velocity of 1–1.6 km/s, denoted by the blue shade, and a later arrival (fundamental mode Scholte waves) with a dominant period of 3–6 s and a velocity of 0.2–0.6 km/s.

2.3 Phase velocity measurements

The fundamental mode Scholte waves are input to a program for Frequency-Time Analysis (FTAN; *Levshin et al.*, 1992; *Levshin and Ritzwoller*, 2001), designed for processing seismic surface wave records through spectral and frequency-time analysis for phase velocity measurements. The longest period that can be measured is restricted to twice the interstation distance (*Bensen et al.*, 2007; *Luo et al.*, 2015). Measurements with low signal-to-noise ratios (< 10) are not used. An associated phase velocity dispersion curve computed from all of the cross-correlation functions following the method proposed by *Park et al.* (1998), and a forward model of phase velocity dispersion curve based on a shear velocity model at site S002 (Figure 1 inset; *Kuo et al.*, 2015), are used as references to unwrap the phase (picking one branch from the measurements). For each station pair, the measured dispersion curves are unwrapped according to which branch is closest to the forward-modeled phase velocities and the high energy of the associated phase velocity (the background colors in Figure 3a). Figure 3 shows an example of phase unwrapping, all the unwrapped phase velocity dispersion curves, and corresponding ray path coverage.

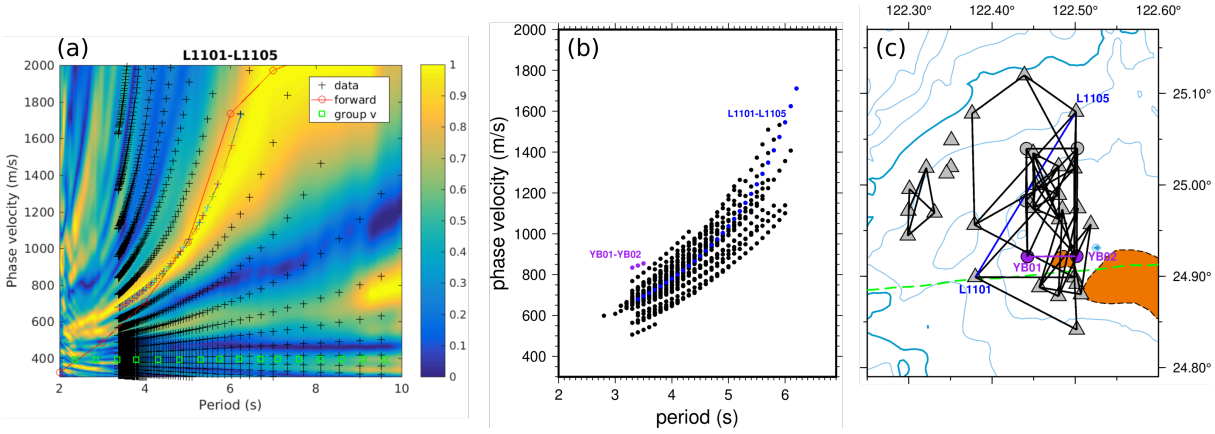

Figure 3. Phase velocities and station-pair path coverage. (a) An example of unwrapping the phase of measurement on station pair L1101-L1105. Black crosses display the measured phase velocities with different cycles, and colored crosses are the chosen phase velocities, corresponding to the blue curve in (b). Its ray path is shown in (c) as blue. Each station pair is picked independently. The background colors show associated phase velocity dispersion energy using all the fundamental mode Scholte waves, following the method proposed by *Park et al.* (1998). The red curve with circles showing its samples denotes the phase velocities predicted by a reference model at site S002 (Figure 1 inset; *Kuo et al.*, 2015). The green squares are group velocities measured by FTAN (*Levshin et al.*, 1992; *Levshin and Ritzwoller*, 2001) (b) 56 Phase velocity dispersion curves measured from the fundamental mode (later arrivals in Figure 2) after unwrapping. (c) Station-pair path coverage of the fundamental mode Scholte waves. The green dashed line indicates the rifting axis. The orange shades mark the volcanic outcrops or slightly buried volcanism (*Sibuet et al.*, 1998). The purple line connecting station pair YB01-YB02 corresponds to the purple curve in (b).

2.4 3D Monte Carlo inversion

We perform fully 3D Monte Carlo tomography using a code (https://github.com/xin2zhang/MCTomo) developed by the Edinburgh Interferometry Project (*Zhang et al.*, 2018, 2020). It uses the reversible jump Markov chain Monte Carlo (rj-McMC) algorithm (*Green*, 1995; *Bodin and Sambridge*, 2009) based on a Bayesian framework to generate samples from the posterior probability density function (pdf) in the 3D model space.

A prior probability density function (pdf) sets the range of shear wave velocities, varying with depth (Figure S3). The range of Vp is set to 1.5-6 km/s. Density is calculated based on Vp according to a typical crustal relationship $\rho = 2.35{+}0.036{\times}(Vp{-}3.0)^2$, where Vp is in km/s and ρ is given in g/cm^3 (*Kurita*, 1973). The program produces model samples within the shear wave velocity range whose phase velocities fit the observations (Figure 3b). We first ran the program using 16 chains of 750,000 samples. The last one of every 50 samples is retained. The first 130,000 iterations were not used to avoid initialization effects. We then ran the program three more times, each with 16 chains producing 450,000 samples, the first 130,000 again being discarded. Misfits are plotted to monitor the convergence of the iterations (Figure S4): misfit curves tend to be flat when the iterations converge after about 10,000-time iterations. The final results are derived from retained samples from 64 chains.

The maximum inversion depth is 4 km below the seafloor. The water depth variation in the inversion area spans about 1.2 km (between 0.39 km and 1.6 km). Therefore, the seabed topography is modeled in the inversion, with the thickness of water depth at each geographic point added to the top of the 3D model.

3 Results

3.1 3D shear velocity structure

After inversion, we obtained a mean 3D shear wave velocity model and corresponding uncertainty estimates. Figure 4 shows some slices through the 3D model at different depths (from 1.75 km to 4.5 km) below the sea level, and Figure 5 shows the corresponding standard deviation. The average water depth in the study region is 1.28 km. The standard deviation (Figure 5) indicates good resolutions down to about 3.5 km below sea level. This is in accordance with the 1D inversion resolution (Chapter 5 in *Wang* (2022)), which indicates a wide range of Vs have high probability density function values below 3.6 km.

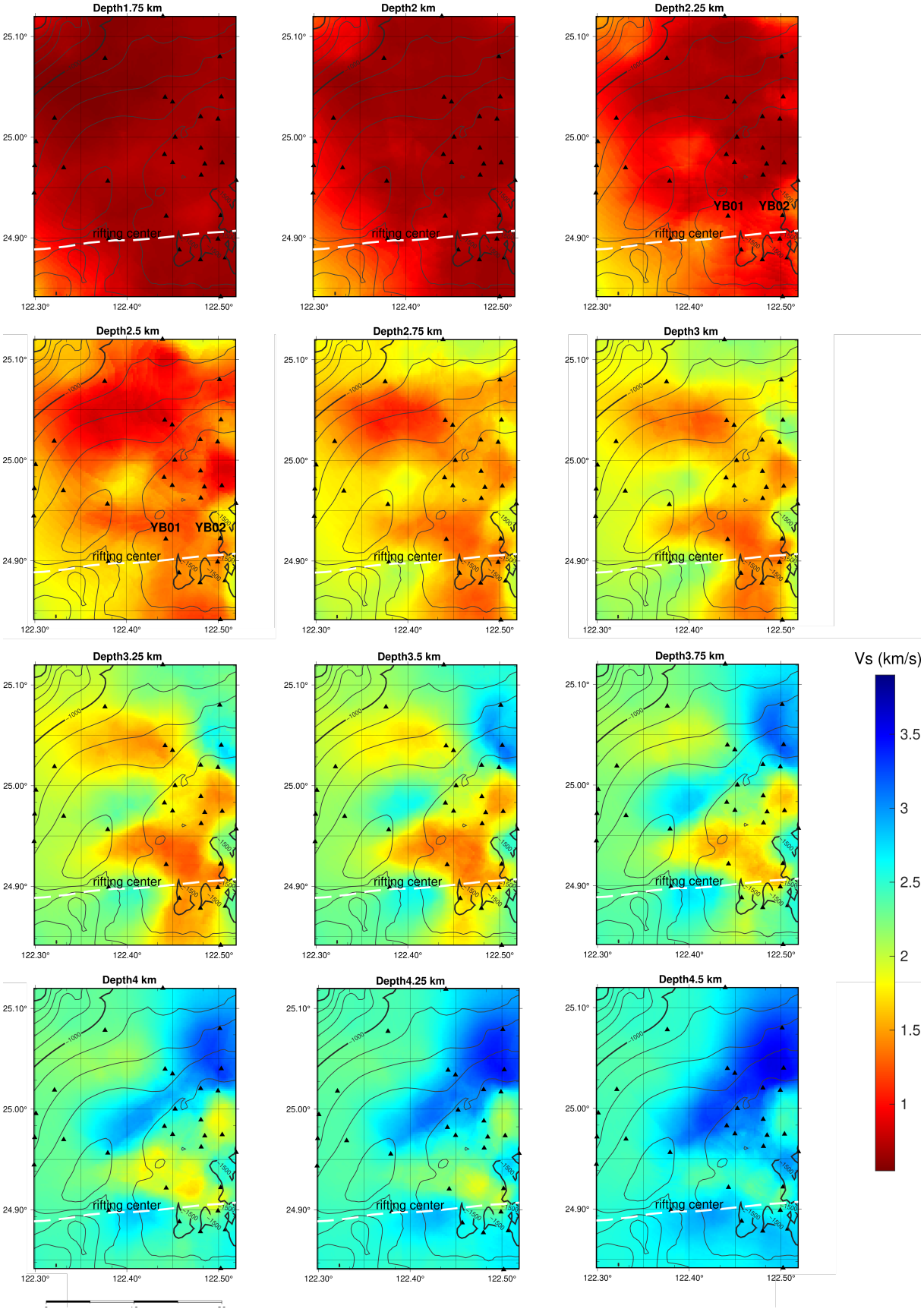

Figure 4. Slices of the mean 3D shear wave velocity model at various depths beneath sea level (water depth is included). Contours indicate the seawater depths. Black triangles indicate the OBSs. Stations YB01 and YB02 are marked on the 2.5 km slice. Panels share the same colorscale.

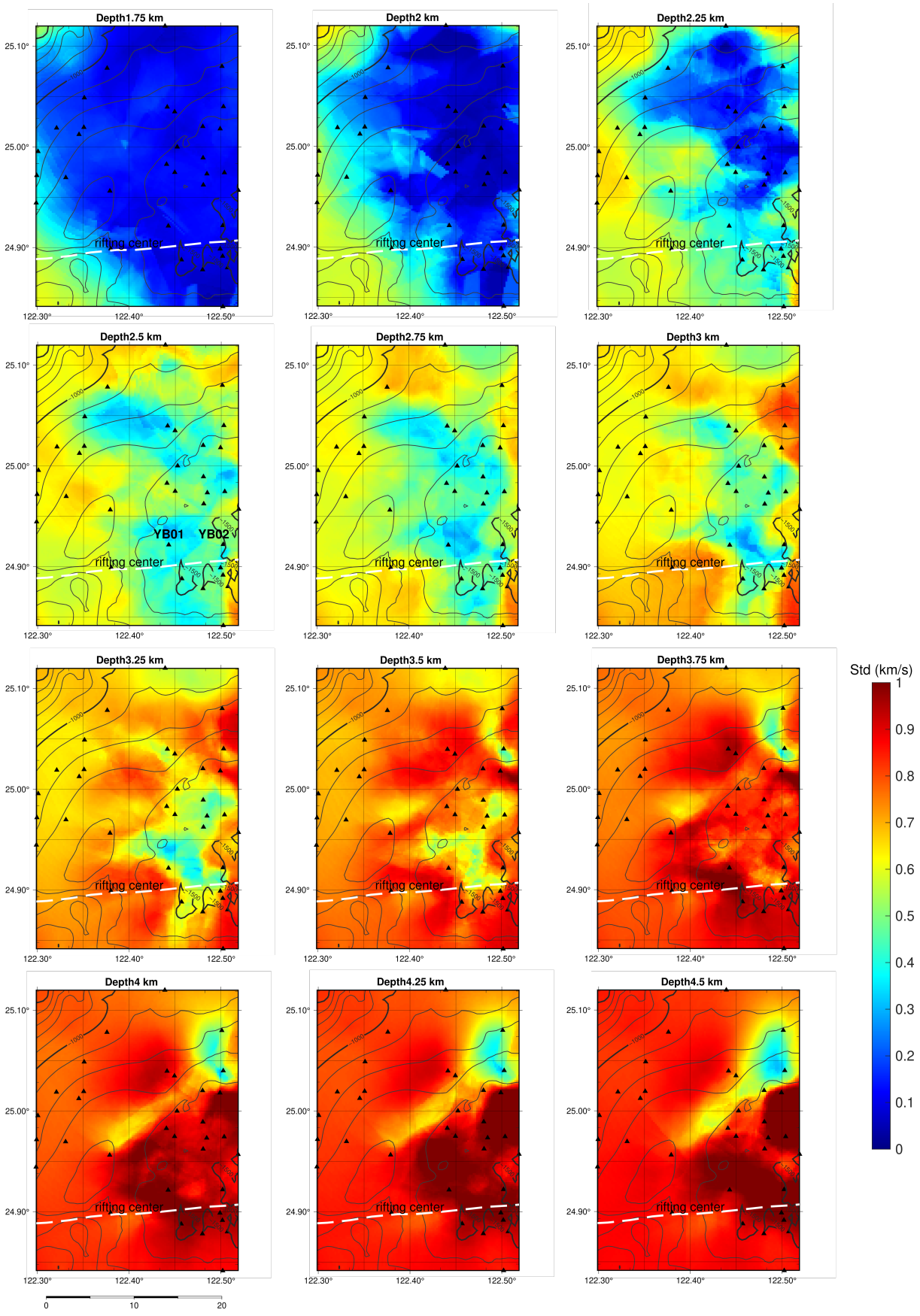

Figure 5. Standard deviations corresponding to Figure 4. Depth is from the sea level (water depth is included). Stations YB01 and YB02 are marked on the 2.5 km slice.

4 Discussion

4.1 Rifting centre

At 1.75 km depth, the velocity is correlated to the water depths (Figure 4): sediments under deeper water (southeast) have higher velocity than sediments under shallower water (northwest). The increase in water pressure can cause this through sediment compaction. We have reasonably low uncertainties on the velocities of the near surface (Figure 5).

Below the sediments, we see the geological structure of the region. From 2.5 km and below, the velocity is low slightly north of the rifting centre, indicating that rifting is active and may terminate at 122.35°E. The corresponding uncertainties are low until down to 3.75 km (Figure 5). The low velocity corresponds to a ridge (Figure 1) on the seafloor, which might indicate the rifting centre in this region. Along the rifting centre, there is volcanism east of the study region (orange shade in Figure 3c). This corresponds to a high velocity from 2.5 km and below (Figure 4), which might represent a cooled magma in the shallow crust, although this is on the edge of the inversion region, so this interpretation is tentative.

From 2.75-3.5 km depth, a low velocity at (122.48°, 24.92°) corresponds to a volcanic outcrop (the small orange shade between YB01-YB02 in Figure 3c), which might be due to extruded lava or melt. The short station-pair path YB01-YB02 only crosses this volcanic outcrop. Its dispersion curve (Figure 3b) shows high phase velocity while the inversion shows low shear velocity. Because the interstation distance is short, we only have short-period phase velocities (3.3–3.5 s) for this station pair. From sensitivity kernels (Figure S5), the periods are only sensitive down to 2 km, while the velocities (between YB01 and YB02) are relatively low at depths deeper than 2.5 km and become relatively high at 2.25 km depth. The high velocity above the low velocity may indicate a hot magma cooled down while moving to the shallower crust. We have reasonably low uncertainties on the velocities between YB01-YB02 (Figure 5). To deeper depth (> 3.75 km), we do not have constraints. Although the high velocities in the northeast (Figure 4) have low uncertainties (Figure 5), the uncertainties of the surrounding area are too high that it is difficult to say that this is a high-velocity anomaly because the velocities in the surrounding area are not reliable.

4.2 Comparison to surrounding regions

The 3D shear velocities are averaged to a 1D profile (Figure 6b). The shear velocities at depths $< 1.6km$ (the max water depth) are only averaged from the values in solid media. We compare our shear velocity with surrounding regions. *Kuo et al.* (2015) analysed seafloor compliance and constrained shear velocity models at S002 and S005 (Figure 6a). Our 1D profile (black curve in Figure 6b) shows a sediment-crust discontinuity of around 1 km. The five-layer models on S002 and S005 also give a ~ 1 km sediment layer. Under the sediment, the shear velocity increases from the east (S005) to the west (this study) in the southwestern Okinawa trough, though the change from S005 to S002 is larger than the change from S002 to our study region. *Kuo et al.* (2012) studied shear wave splitting from S005 to the site same as our study region, and to northeast Taiwan. They observed an anisotropy decrease from S005 to our study region. Both shear wave velocity increase and anisotropy

decrease support the scenario that the rifting and extension taper towards Taiwan, causing a decreasing degree of stretching and faulting of the upper crust.

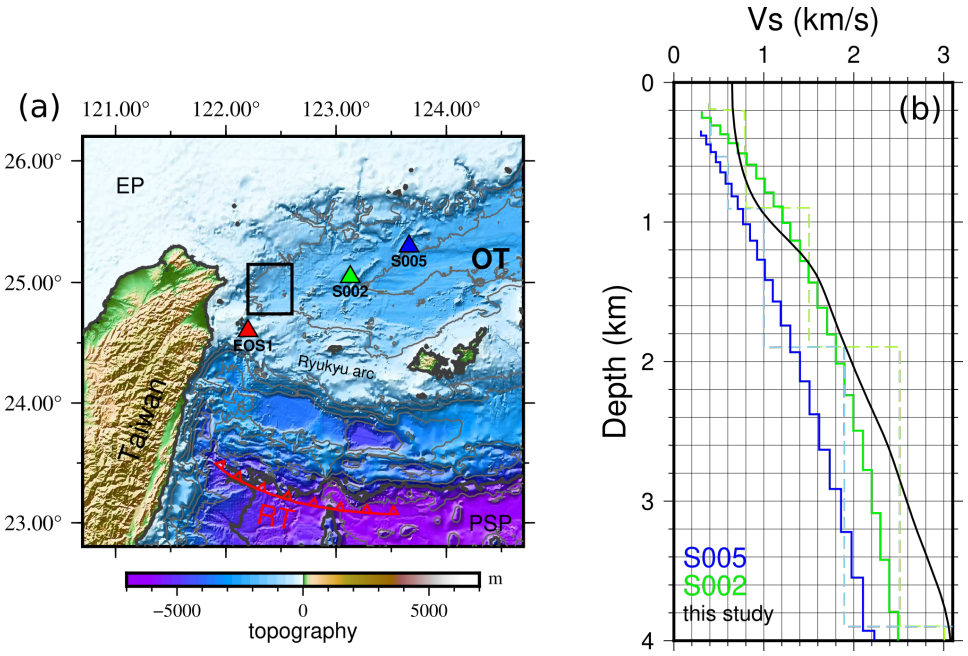

Figure 6. (a) Locations of S005, S002, and the deployment of this study (rectangle). (b) 1D shear velocity comparing with S002 and S005 (*Kuo et al.*, 2015). The dashed lines present the layer version of Vs on S002 (green) and S005 (blue). Depth is from the seabed (water depth is not included).

5 Conclusions

This study focuses on a region (~ 0.2°×0.3°) of the western Okinawa Trough with a dense deployment (2–10 km inter-station distance). Two arrivals of Scholte waves are retrieved from both seismic vertical channels and pressure gauges. Phase velocities are measured from the fundamental mode Scholte waves (the later arrivals). Several references, including phase velocity dispersion energy and a reference phase velocity dispersion curve forwarded based on an adjacent site S002 (*Kuo et al.*, 2015), are used for phase unwrapping. 3D shear wave velocity structure in the upper crust of the southwestern Okinawa Trough is constrained using 3D Monte Carlo inversion. The low velocity slightly north of the rifting centre indicates the rifting is active at the southwest edge of Okinawa Trough. Comparing to a previous study (*Kuo et al.*, 2015), the shear velocity increases from east to west in the southwestern Okinawa trough, which may indicate the back-arc rifting and extension taper towards Taiwan.

Acknowledgments

We acknowledge the Institute of Earth Sciences, Academia Sinica, for providing all the OBS data used in this study. The author acknowledges the support from an Endeavour Fund grant (funding contract C05X1605) from the Ministry of Business, Innovation and Employment, New Zealand. The 3D inversion was performed under the Project HPC-EUROPA3 (INFRAIA-2016-1-730897), with the support of the EC Research Innovation Ac-

tion under the H2020 Programme; we acknowledge the support from the School of Geosciences, the University of Edinburgh, and the computer resources and technical support provided by EPCC - The University of Edinburgh. We also acknowledge Aleksandr Beliaev for IT support.

References

Bensen, G., M. Ritzwoller, M. Barmin, A. L. Levshin, F. Lin, M. Moschetti, N. Shapiro, and Y. Yang (2007), Processing seismic ambient noise data to obtain reliable broad-band surface wave dispersion measurements, *Geophysical Journal International*, *169*(3), 1239–1260.

Bodin, T., and M. Sambridge (2009), Seismic tomography with the reversible jump algorithm, *Geophysical Journal International*, *178*(3), 1411–1436.

Chen, L., H.-T. Chiang, J.-N. Wu, L.-Y. Chiao, C.-T. Shyu, C.-S. Liu, Y. Wang, and S.-C. Chen (2020), The focus thermal study around the spreading center of southwestern Okinawa trough, *Tectonophysics*, *796*, 228,649.

Chou, H.-C., B.-Y. Kuo, S.-H. Hung, L.-Y. Chiao, D. Zhao, and Y.-M. Wu (2006), The Taiwan-Ryukyu subduction-collision complex: Folding of a viscoelastic slab and the double seismic zone, *Journal of Geophysical Research: Solid Earth*, *111*(B4).

Chou, H.-C., B.-Y. Kuo, L.-Y. Chiao, D. Zhao, and S.-H. Hung (2009), Tomography of the westernmost Ryukyu subduction zone and the serpentinization of the fore-arc mantle, *Journal of Geophysical Research: Solid Earth*, *114*(B12).

Green, P. J. (1995), Reversible jump Markov chain Monte Carlo computation and Bayesian model determination, *Biometrika*, *82*(4), 711–732.

Han, B., X. Zhang, J. Pei, and W. Zhang (2007), Characteristics of crust-mantle in East China sea and adjacent regions, *Progress in Geophysics*, *22*(2), 376–382.

Jia, X., and D. Sun (2021), Imaging the crustal interfaces along the Ryukyu arc-trough system using precursors to teleseismic sP and pP, *Journal of Geophysical Research: Solid Earth*, *126*(2), e2020JB020,413.

Kearey, P., K. Klepeis, and F. Vine (2009), Global Tectonics, 3rd editions.

Kinoshita, M., and M. Yamano (1997), Hydrothermal regime and constraints on reservoir depth of the Jade site in the Mid-Okinawa Trough inferred from heat flow measurements, *Journal of Geophysical Research: Solid Earth*, *102*(B2), 3183–3194.

Ko, Y.-T., B.-Y. Kuo, K.-L. Wang, S.-C. Lin, and S.-H. Hung (2012), The southwestern edge of the Ryukyu subduction zone: A high Q mantle wedge, *Earth and Planetary Science Letters*, *335*, 145–153.

Kuo, B.-Y., C.-C. Wang, S.-C. Lin, C.-R. Lin, P.-C. Chen, J.-P. Jang, and H.-K. Chang (2012), Shear-wave splitting at the edge of the Ryukyu subduction zone, *Earth and Planetary Science Letters*, *355*, 262–270.

Kuo, B.-Y., W. C. Crawford, S. C. Webb, C.-R. Lin, T.-C. Yu, and L. Chen (2015), Faulting and hydration of the upper crust of the SW Okinawa Trough during continental rifting: Evidence from seafloor compliance inversion, *Geophysical Research Letters*, *42*(12), 4809–4815.

Kurita, T. (1973), Regional variations in the structure of the crust in the central United States from P-wave spectra, *Bulletin of the Seismological Society of America*, *63*(5), 1663–1687.

Lecocq, T., C. Caudron, and F. Brenguier (2014), MSNoise, a python package for monitoring seismic velocity changes using ambient seismic noise, *Seismological Research Letters*, *85*(3), 715–726.

Levshin, A., and M. Ritzwoller (2001), Automated detection, extraction, and measurement of regional surface waves, in *Monitoring the comprehensive nuclear-test-ban treaty: Surface waves*, pp. 1531–1545, Springer.

Levshin, A., L. Ratnikova, and J. Berger (1992), Peculiarities of surface-wave propagation across central Eurasia, *Bulletin of the Seismological Society of America*, *82*(6), 2464–2493.

Lin, S.-C., and B.-Y. Kuo (2013), Trench-parallel flow in the southern Ryukyu subduction system: Effects of progressive rifting of the overriding plate, *Journal of Geophysical Research: Solid Earth*, *118*(1), 302–315.

Liu, B., S.-Z. Li, Y.-H. Suo, G.-X. Li, L.-M. Dai, I. Somerville, L.-L. Guo, S.-J. Zhao, and S. Yu (2016), The geological nature and geodynamics of the Okinawa Trough, Western Pacific, *Geological Journal*, *51*, 416–428.

Luo, Y., Y. Yang, Y. Xu, H. Xu, K. Zhao, and K. Wang (2015), On the limitations of interstation distances in ambient noise tomography, *Geophysical Journal International*, *201*(2), 652–661.

Nakamura, M. (2004), Crustal deformation in the central and southern Ryukyu Arc estimated from GPS data, *Earth and Planetary Science Letters*, *217*(3-4), 389–398.

Nishimura, S., M. Hashimoto, and M. Ando (2004), A rigid block rotation model for the GPS derived velocity field along the Ryukyu arc, *Physics of the Earth and Planetary Interiors*, *142*(3-4), 185–203.

Nolet, G., and L. M. Dorman (1996), Waveform analysis of Scholte modes in ocean sediment layers, *Geophysical Journal International*, *125*(2), 385–396.

Park, C. B., R. D. Miller, and J. Xia (1998), Imaging dispersion curves of surface waves on multi-channel record, in *SEG Technical Program Expanded Abstracts 1998*, pp. 1377–1380, Society of Exploration Geophysicists.

Ramsey, L., N. Hovius, D. Lague, and C.-S. Liu (2006), Topographic characteristics of the submarine Taiwan orogen, *Journal of Geophysical Research: Earth Surface*, *111*(F2).

Salisbury, e. a., M. H. (2002), Proceedings of the Ocean Drilling Program, *Init. Rep.*, *195*(3).

Seno, T., S. Stein, and A. E. Gripp (1993), A model for the motion of the Philippine Sea plate consistent with NUVEL-1 and geological data, *Journal of Geophysical Research: Solid Earth*, *98*(B10), 17,941–17,948.

Shyu, C.-T., and C.-S. Liu (2001), Heat flow of the southwestern end of the Okinawa Trough, *TERRESTRIAL ATMOSPHERIC AND OCEANIC SCIENCES*, *12*(SUPP), 305–318.

Sibuet, J.-C., and S.-K. Hsu (2004), How was Taiwan created?, *Tectonophysics*, *379*(1-4), 159–181.

Sibuet, J.-C., J. Letouzey, F. Barbier, J. Charvet, J.-P. Foucher, T. W. Hilde, M. Kimura, L.-Y. Chiao, B. Marsset, C. Muller, et al. (1987), Back arc extension in the Okinawa Trough, *Journal of Geophys-*

ical Research: Solid Earth, *92*(B13), 14,041–14,063.

Sibuet, J.-C., S.-K. Hsu, C.-T. Shyu, and C.-S. Liu (1995), Structural and kinematic evolutions of the Okinawa Trough backarc basin, in *Backarc basins*, pp. 343–379, Springer.

Sibuet, J.-C., B. Deffontaines, S.-K. Hsu, N. Thareau, J.-P. Le Formal, and C.-S. Liu (1998), Okinawa trough backarc basin: Early tectonic and magmatic evolution, *Journal of Geophysical Research: Solid Earth*, *103*(B12), 30,245–30,267.

Su, P.-L., P.-F. Chen, and C.-Y. Wang (2019), High-resolution 3-DP wave velocity structures under NE Taiwan and their tectonic implications, *Journal of Geophysical Research: Solid Earth*, *124*(11), 11,601–11,614.

Wang, W. (2022), Studies of Seismic Velocities in Subduction Zones from Continuous Ocean Bottom Seismometer Data, Ph.D. thesis, Open Access Te Herenga Waka-Victoria University of Wellington.

Yamano, M., S. Uyeda, J.-P. Foucher, and J.-C. Sibuet (1989), Heat flow anomaly in the middle Okinawa Trough, *Tectonophysics*, *159*(3-4), 307–318.

Yu, Z., S. Zhai, K. Guo, Y. Zhou, and T. Zong (2016), Helium isotopes in volcanic rocks from the Okinawa Trough—impact of volatile recycling and crustal contamination, *Geological Journal*, *51*, 376–386.

Zhang, X., A. Curtis, E. Galetti, and S. De Ridder (2018), 3-D Monte Carlo surface wave tomography, *Geophysical Journal International*, *215*(3), 1644–1658.

Zhang, X., F. Hansteen, A. Curtis, and S. de Ridder (2020), 1-D, 2-D, and 3-D Monte Carlo Ambient Noise Tomography Using a Dense Passive Seismic Array Installed on the North Sea Seabed, *Journal of Geophysical Research: Solid Earth*, *125*(2), e2019JB018,552.

Supporting Information for 3D shear wave velocity structure in the southwestern Okinawa Trough

Weiwei Wang[1,2], Shu-Huei Hung[2], Martha K. Savage[1], Yinhe Luo[3], Xin Zhang[4], Andrew Curtis[4], Spahr Webb[5], Ban-Yuan Kuo[6], Tim Stern[1], Xiaozhou Yang[3], Jinyun Xie[3], Hsin-Ying Yang[2], Pei-Ying Patty Lin[7], Chau-Chang Wang[8,9], Ching-Ren Lin[6]

[1]Victoria University of Wellington, Wellington, New Zealand

[2]National Taiwan University, Taipei, Taiwan

[3]China University of Geosciences (Wuhan), Wuhan, China

[4]The University of Edinburgh, Edinburgh, UK

[5]Lamont-Doherty Earth Observatory, Columbia University, Palisades, NY, USA

[6]Institute of Earth Sciences, Academia Sinica, Taipei, Taiwan

[7]National Taiwan Normal University, Taipei, Taiwan

[8]National Sun Yat-Sen University, Kaohsiung, Taiwan

[9]Taiwan Ocean Research Institute, Kaohsiung, Taiwan

Contents of this file

1. S1: Deployment; S2: 3D inversion
2. Table S1 to S2
3. Figures S1 to S4

Introduction

The supporting information contains additional details about data and analysis to support the Data and method section in the main text.

S1. Deployment

The locations of the OBSs used in this study can be found in Table S1. The OBSs are of two types: one is called Lobster from Germany, and the other one is called Yarbird from IES. Yarbird instruments were produced by IES and have been frequently updated since 2010. We name different types of Yarbird instruments according to the low corner frequency of the instrument response, i.e., if the low corner frequency is 3 s, the instrument is called Yarbird-3s. Among the 34 OBSs, 5 of them are only equipped with 3-component seismometers, and 29 of them are equipped with differential pressure gauges and 3-component seismometers.

Table S2 shows the information about the deployment and different types of instruments, and Figure S1 shows the corresponding instrument responses. As all the instruments use the same differential pressure gauge type, instrument responses of differential pressure gauges are not considered during data processing. Instrument responses of seismic vertical components are only removed if the instruments deployed during the same time are different types. Figure S2 shows an example of power spectral density from this study.

Table S1. Locations of the ocean bottom seismometers used in this study.

Station	Longitude	Latitude	Altitude (m)
YB01	122.4426	24.9216	-1492
YB02	122.5019	24.9220	-1514
YB03	122.4407	24.9828	-1452
YB04	122.4414	25.0396	-1255
YB05	122.5026	25.0400	-1373
L1101	122.380	24.8990	-1300
L1102	122.499	24.8988	-1503
L1104	122.499	25.0180	-1427
L1105	122.501	25.0799	-1213
L1106	122.439	25.1199	-1014
Y1102	122.502	24.8415	-1370
Y1103	122.379	24.9563	-1265
Y1105	122.376	25.0781	-1111
Y1507	122.3512	25.0487	-1129
Y1508	122.3507	25.0194	-1220
Y1509	122.5017	24.8916	-1521
Y1601	122.3210	25.0188	-1119
Y1602	122.3454	25.0124	-1185
Y1603	122.3008	24.9955	-1136
Y1604	122.2994	24.9717	-1159
Y1605	122.3310	24.9696	-1225
Y1606	122.2988	24.9445	-1243
Y1701	122.4495	25.0349	-1267
Y1702	122.4801	25.0203	-1390
Y1703	122.4523	25.0000	-1415
Y1704	122.4804	24.9892	-1435
Y1705	122.4496	24.9748	-1426
Y1706	122.4807	24.9623	-1466
Y1801	122.4846	24.9733	-1462
Y1802	122.5036	24.9745	-1509
Y1803	122.5188	24.9570	-1550

Station	Longitude	Latitude	Altitude (m)
Y1804	122.4569	24.8880	-1485
Y1805	122.5070	24.8802	-1579
Y1806	122.4799	24.8782	-1496

Table S2. Deployment and instrumentation information. Yarbird uses the same type of differential pressure gauge as Lobster. The max number of cross-correlations (CC) is computed by permutation C_n^2, where n is the number of stations during the same time period, 2 stands for 'every 2 stations compute one CC'. CC: cross-correlations; BB: Broadband.

Time	Number of stations	Max number of CC	Instrument type
2010.06–2010.09	5	10	Yarbird-3s
2011.09–2012.08	8	28	3 Yarbird-7s, 5 Lobster
2015.11–2016.04	3	3	Yarbird-BB
2016.08–2017.04	6	15	Yarbird-BB
2017.06–2017.10	6	15	Yarbird-BB
2018.04–2018.06	6	15	Yarbird-BB
In total	34	86	

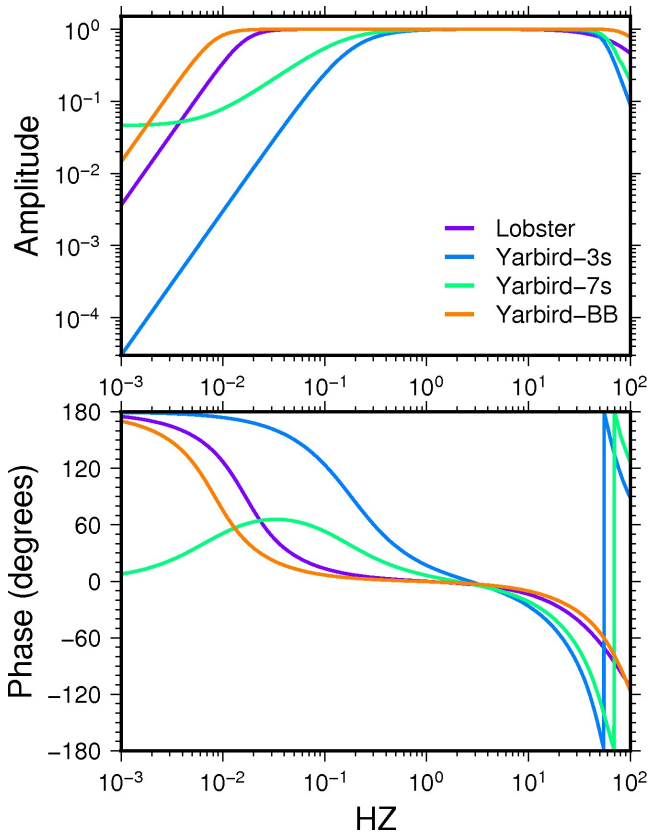

Figure S1. Velocity responses of the vertical components of different instruments deployed in southwestern Okinawa Trough with amplitude normalized to 1, corresponding to the instrument types in Table S2.

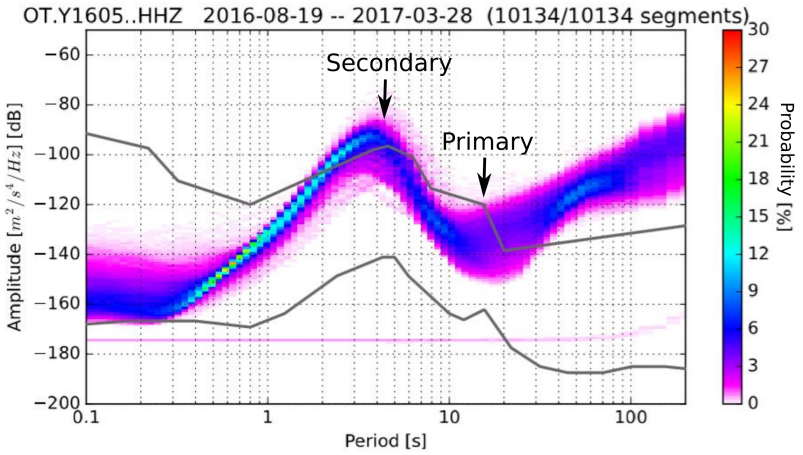

Figure S2. Power spectral density of ambient noise recorded at Y1605. The worldwide high and low noise levels from land stations (*Peterson et al.*, 1993) are shown by grey curves for comparison. The two arrows mark the peaks of primary microseism and secondary microseism.

S2. 3D inversion

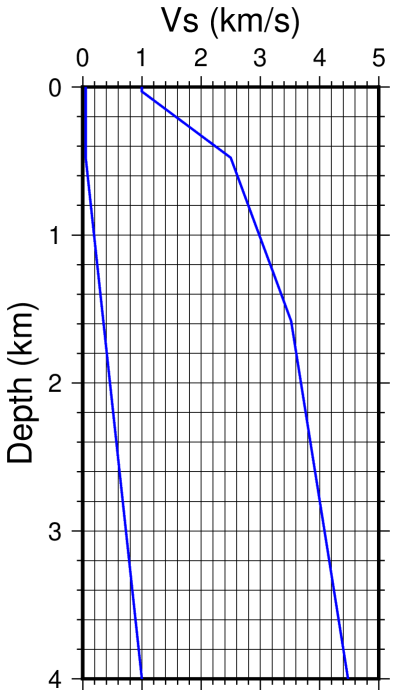

Figure S3. Prior setting for Vs inversion. The two blue curves indicate the Vs search range.

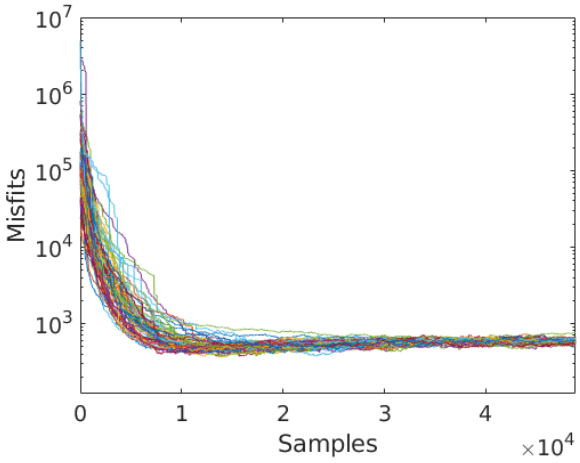

Figure S4. Misfits convergence along the iterations (samples). The x-axis does not present all the iterations, which is 750,000. Different colors present different chains (64 chains in total).

S0.1 Sensitivity kernels

The 3D shear velocities are averaged to a 1D profile (Figure S5a). The shear velocities at depths $< 1.6km$ (the max water depth) are only averaged from the values in solid media. Linearised sensitivity kernels of fundamental mode Scholte wave phase velocities are computed based on the 1D shear velocity profile (Figure S5b). The kernels show sensitivity down to 4 km, indicating that inversion results down to 4 km (including the water layer) are valid, which is in accordance with the standard deviation (Figure 5).

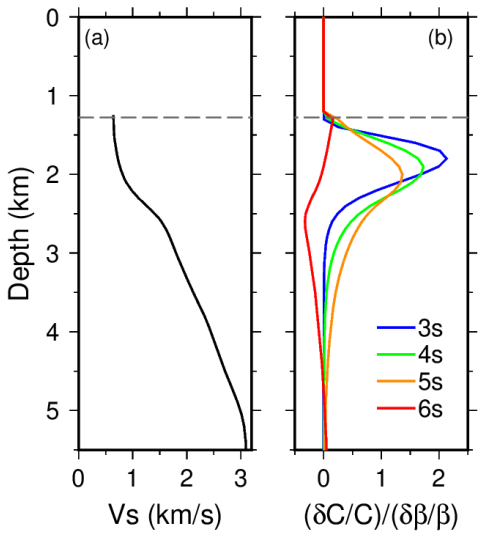

Figure S5. (a) 1D shear velocity averaged from the 3D shear velocity (Figure 4); (b) Sensitivity kernels of fundamental mode Scholte wave phase velocities, based on the 1D shear velocity model. Depth is from the sea level (water depth is included, denoted by a grey dashed line).

References

Peterson, J., et al. (1993), Observations and modeling of seismic background noise.